7-7-2005

Sub-surface corrosion research on rock bolt system, perforated SS sheets and steel sets for the Yucca Mountain Repository — Quarterly technical report No. 4

Dhanesh Chandra
University of Nevada, Reno, dchandra@scs.unr.edu

Jaak J.K. Daemen
University of Nevada, Reno, daemen@mines.unr.edu

"Sub-surface Corrosion Research on Rock Bolt System, Perforated SS Sheets and Steel Sets for the Yucca Mountain Repository"

Quarterly Technical Report No. 4 (2tnd Quarter of FY 2005)

Start Date of this Quarter, April 1, 2005 to June 30, 2005

Task No: ORD-FY04-019 and Document No: SIP-UNR-040

Prepared for U.S. DOE/UCCSN Cooperative Agreement Number DE-FC28-04RW12232

-submitted to-

United States Department of Energy
Office of Civilian Defense Radioactive Waste Management
Yucca Mountain Project
1551 Hillshire Drive, Suite A
Las Vegas NV 89134-6321

and

Harry Reid Center
University of Nevada, Las Vegas
4505 Maryland Parkway
Las Vegas Nevada 89154-4009

-submitted by-

Metallurgical and Materials Engineering
Mail Stop 388
1664 N. Virginia Street
College of Engineering
University of Nevada, Reno
Reno NV 89557

Dhanesh Chandra, PI (Corrosion Team Leader)
Jaak Daemen (Co-PI)

July 7, 2005

Task ORD-FY04-019 "Sub-surface Corrosion Research on Rock Bolt System, Perforated SS Sheets and Steel Sets for the Yucca Mountain Repository"
(A Quality-Affecting Task)
Principal Investigator, Dhanesh Chandra
DOE Technical Representative, Jaime Gonzalez
Quarterly Technical Progress Report
04/01/05 - 06/30/05

Statement of Work

The objective of this task is to conduct corrosion related research and predict the durability of rock-bolts and other underground metallic roof supports. In this period, we have performed oxidation tests of Split Set, Swellex Mn24, Williams rock bolts, and Alloy 22 (baseline material) specimens, potentiodynamic tests, characterization of alloys.

General Statements

- Corrosion rates of the rock bolts have been obtained using electrochemical Potentiodynamic scans using YM environment electrolytes.
- Baseline Corrosion Rates have been established for Alloy 22 using YM waters. Characterization of dry oxidation tests using scanning electron microscopy on oxidized samples in a TGA of Alloy 22 (wrought condition) show that the initial weight loss is mainly due to grain boundary precipitation of phases similar to those of TCP phases.

Progress for the Period 04/01/05-06/30/05:

Subtask 1: Selection of New High Strength Steels, Stainless Steels for Rock Bolts, Steel Sets and Perforated Roof Supports
Subtask 2: Electrochemical tests to evaluate corrosion rate and possible corrosion mechanisms
Subtask 3. Electrochemical Impedance Spectroscopy (EIS)
Subtask 5: .Hydrogen Permeation tests
Subtask 7: Dry Oxidation Tests by Thermogravimetric analyses
Subtask 8: Microstructure and Phase Characterization Studies

Two peer reviewed *Journal papers* have been published in this quarter:

1. "Electrochemical Corrosion Behavior of Low Carbon I-beam steels in a Simulated Yucca Mountain Repository Environment," V. Arjunan, J. Lamb, D. Chandra, J. Daemen, D. Jones, M. Engelhard, and S. Lea, Published in *Corrosion (NACE)* vol. 61, No.4, April, 2005, 381-391
2. "Corrosion Behavior of Carbon Steel Rock Bolt in Simulated Yucca Mountain Ground Waters," A. Yilmaz, D. Chandra, and R.B. Rebak, Published in *Metallurgical Transactions* A, (TMS), vol. 36A, May 2005, 1097-1105.

Two presentations in the NACE Corrosion National Conference in Houston Texas, April 21-25, 2005:

1. "Isothermal Oxidation Studies on Ni-Based Superalloy at Moderately Elevated Temperatures," Anjali Talekar, Dhanesh Chandra, Raja Chellappa, Wen-Ming Chien, Raul Rebak, *Corrosion 2005, NACE Conference* Houston, Texas April 3-7 , 2005.
2. "Stress Corrosion Cracking/Hydrogen Embrittlement Study of Nickel Alloy 22," Sazzadur Rahman, Joshua Lamb, Dhanesh Chandra, Raul Rebak, *Corrosion 2005, NACE Conference"*, Houston, Texas April 3-7, 2005.

1. INTRODUCTION

This report encompasses the work done for this third quarter, 2005, in accordance to cooperative agreement of University of Nevada system for the Task 019 "Subsurface Corrosion Research on Rock Bolt System, Perforated SS Sheets and Steel Sets for the Yucca Mountain Repository", the overall objective of which is to conduct corrosion research and predict the durability of rock-bolts and other underground metallic roof supports. We have started oxidation tests using Thermogravimetric Analyzer (TGA), and Potentiodynamic tests to determine the corrosion rates of rock bolts, other support materials including bench mark materials.

In this quarter, we have also performed hydrogen permeation tests on Williams rock bolts (from YM site). We discuss "dry" oxidation of rock bolt steels and other supporting materials that are susceptible to oxidation under the repository conditions. Swellex rock bolts (made by Atlas Copco) and Split Sets rock bolt (HSLA steel made by "International Rollforms") were tested up to 500°C using Modulated Thermogravimetric Analysis (MTGA) method under pure O_2 atmosphere. In addition, a mechanism for weight loss in initial stages isothermal oxidation test of Alloy 22 in pure O_2 atmosphere 980°C using standard TGA was also determined (the experiments were reported in the last quarterly report). It has been concluded that this initial weight loss is primarily due to formation TCP phases on grain boundaries; proof of which is shown in scanning electron micrographs.

2. ROCK BOLT MATERIALS

Folded steel tube closed at both extremities, with a small unique hole for inflation. The bolt is expanded inside a drilled hole through the application of high water pressure inside the bolt. The expansion creates a combination of

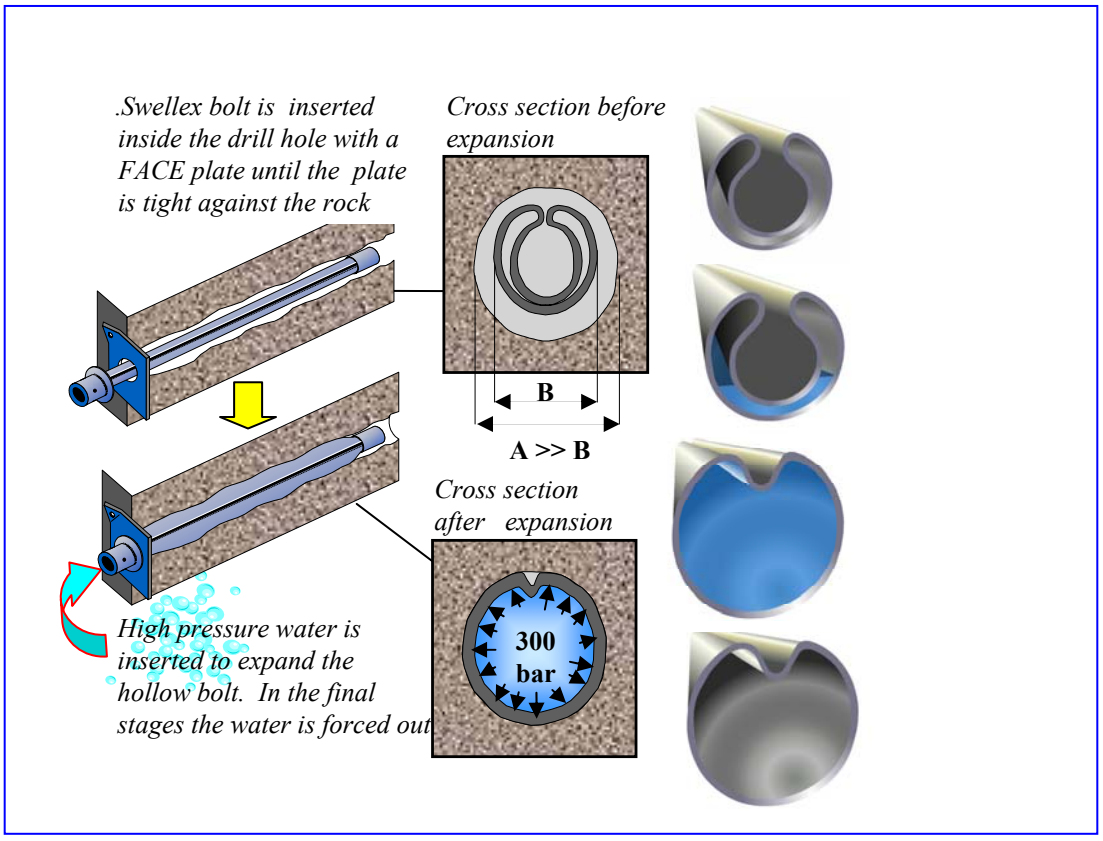

.

Figure2B.2. Swellex Rock bolts in as received condition (left), in as received and cut, and expanded state (middle), a metallographic sample for Potentiodynamic tests (right).

radial compression (creating friction) and mechanical interlocking between the rock asperities and the steel tube surface. The inflation is effectively forming the tube inside the borehole and a high residual pressure is remaining after releasing the water, thus assuring a good friction and an ability to accommodate rock mass relaxation without significant anchorage loss.

Table 2.1 Chemical Composition of Alloy 22 from the Manufacturer.

	Weight Percent (Nominal composition listed by Haynes Corporation)												
	Element	Ni	Co	Cr	Mo	W	Fe	Si	Mn	C	P	S	V
Hastalloy C-22 (Nominal Composition)	% composition	56.6	1.05	21.38	13.55	3.07	3.88	0.028	0.24	0.005	0.006	0.0057	0.14

Table 2.2 Chemical Composition of the Alloys used in this study

Weight Percent of the Actual samples used in this study (Analyzed by QA Qualified Vendor Laboratory Testing Inc. (LTI)														
Alloy	Ni	Co	Cr	Mo	W	Fe	Si	Mn	C	P	S	V		
Hastealloy C-22	56.858	1.00	21.2	13.50	3.00	3.9	0.05	0.31	0.002	0.01	0.01	0.16	-	-
Split set (ASTM A607-98, Grade 50)	0.06		0.02	0.03		98.75		0.68	0.07	0.01	0.01	V .038	Cb/Nb 0.007	Cu+Ni+Cr+Mo 0.22
Swellex Mn-24	0.05	-	0.042	0.027		98.074	0..24	1.16	0.16	0.013	0.004	Al 0.054	Cu 0.17	N 0.006

Table 2.3. Technical data on Swellex Mn-24 rock bolts.

TECHNICAL DATA	GENERAL DATA
Type of steel……EN10 025-S355JR	Profile diameter……..36mm
Minimum breaking load, expanded profile ……200kN*	Material thickness…….....3mm
Typical breaking load, expanded profile…….……240kN*	Original tube diameter……..54mm
Minimum elongation, expanded profile, A_5……..…..20%*	Upper bushing, diameter……38mm
Typical elongation, expanded profile, $A_{5..}$……..30%*	Bushing head, diameter……41/48mm
Minimum breaking load, weld bushing ……..200kN	Recommended hole diameter..43-52mm
Inflation pressure……..…….30Mpa	Optimal hole diameter…….45-51mm

Typical elongation, expanded profile, $A_{5..}$……..30%*	Bushing head, diameter……41/48mm
Minimum breaking load, weld bushing ……..200kN	Recommended hole diameter..43-52mm
Inflation pressure……..…….30Mpa	Optimal hole diameter…….45-51mm

* According to SS-EN 10 002-1 where applicable

3. RESULTS AND DISCUSSION

In this quarter we present Thermogravimetric* and Stress Corrosion Cracking, electrochemical studies (of Alloy 22) results on the following materials:

1. Rock Bolts*: 1. *William Type rock bolts* (medium carbon steel) 2. *International Roll Forms (IRF) - Friction type Split Sets* (HSLA steel), Swellex Mn-24 (Atlas Copco).
2. Baseline Materials: *Alloy 22** (Ni based superalloy) TGA and electro-mechanical studies.

3.1. Task No. 7- Dry Oxidation Tests on Rock bolts and Baseline Alloys

3.1.1. Introduction

High temperature oxidation kinetics and stability of the rock bolts has been performed using dry and pure O_2 in this study using Thermogravimetric analyses to measure the amount of sample mass change as a function of temperature and time. It is traditionally used to characterize any material that exhibits weight loss or phase changes as a result of decomposition, dehydration, and oxidation. In conventional TGA, two modes are commonly used for investigating thermal stability behavior in controlled atmosphere: (1) Dynamic, in which the temperature is increased at a linear rate, and (2) Isothermal, in which the temperature is kept constant. Most of the literature available on oxidation of steels or Ni-based alloys focuses on determination of isothermal reaction kinetics mechanism. The determination of non-isothermal kinetic parameters of oxidation is not a trivial problem, nevertheless important for many practical situations.

At UNR, we have a state-of-the-art Thermogravimetric analyzer from TA Instruments, Model Q500, with a continuous weighing capacity of 1.0 g, a sensitivity of 0.1 μg and a heating rate from 0.1 to 50°C/min. The TA Q500 is also equipped with the ability to perform *Temperature Modulated TGA* (MTGA) with a Hi-Res™ option. The use of MTGA technique has been reported in literature for determining the kinetics of decomposition of materials (ceramics and polymers) termed as weight-loss experiments. However, the use of MTGA has not been reported for the study of oxidation kinetics of metals or alloys. In this report, we present the MTGA results for baseline dry oxidation experiments performed on three steel samples: International Rollforms Split Set (HSLA) [AN-SS46-T-1-3], Williams Rock Bolt [An-RB-01014622-2] and Swellex Mn-24 [Mn24-tga1]. We note here that the experiments were conducted in relatively low temperature regimes to understand instrumental behavior and to aid the design of future experiments.

3.1.2. Experimental

All Thermogravimetric experiments in this quarter were performed using the temperature modulated option. For this, the furnace was changed to the standard furnace and weight as well as temperature calibration was performed again. The use of standard furnace ensures the close coupling between the test specimen, furnace and temperature sensor required for rapid temperature modulation. The temperature profile MTGA is typically a superposition of a sinusoidal modulation with an underlying heating rate and is given by:

$$T(t) = T_0 + \beta_{avg} t + A_T \sin\left(\frac{P}{2\pi} \cdot t\right) \tag{3.1.1}$$

where, T_0 is the initial start temperature, β_{avg} is the average or underlying heating rate (2°C/min), A_T is the modulation amplitude (±5°C), P is the period (1/200 cycles per sec). The following experimental parameters were used for all the experiments:

1: Modulate +/- 5.00°C every 200 seconds
2: Ramp 2.00°C/min to T°C (typically 500°C)
3: End of method

Alumina sample pans were used and a flow rate of 40:60 ml/min to balance and furnace respectively of high purity oxygen gas was maintained. All the samples were polished to a 0.03 micron finish as best as possible (the size of the sample being the delimiting factor). These samples were then thoroughly washed in D.DI water and put in an ultrasonic cleaner for 5min and thereafter allowed to dry for atleast 30-40 min or more. They were then introduced into the furnace on tared pans and the set-up was allowed to equilibrate for 20 minutes before starting the experiment.

3.1.3. Determination of Non-isothermal Oxidation Kinetics

MTGA experiments similar to those conducted in this study can be designed to understand the high temperature non-isothermal kinetics of steels and alloys. In this section, a brief description of the procedure that can be used to determine non-isothermal kinetic parameters is provided. The differential form of the non-isothermal rate equation is [1]:

$$\frac{d\alpha}{dT} = \frac{A}{\beta}\exp\left(\frac{-E_a}{RT}\right) f(\alpha) \tag{3.1.2}$$

where, α is the reaction fraction (can be defined in different ways, it is defined as weight gain per unit surface area ($\Delta m/A_{surf}$) for present purposes), A is the Arrhenius pre-exponential factor, E_a is the activation energy, β is the derivative of the heating profile (dT/dt), $f(\alpha)$ is the kinetic expression determining the order of the reaction, R is the gas constant, and T is the temperature.

The expression given in equation (3.1.2) can also be expressed in terms of the rate of reaction:

$$\beta\frac{d\alpha}{dT} = \frac{d\alpha}{dt} = A\exp\left(\frac{-E_a}{RT}\right) f(\alpha) \tag{3.1.3}$$

The integral form of the non-isothermal rate equation is (from ref.1):

$$g(\alpha) = A\int_0^T \frac{1}{\beta}\exp\left(\frac{-E_a}{RT}\right) dT \tag{3.1.4}$$

The problem of obtained 'E', 'A', and "$f(\alpha)$' is called a triplet problem. By performing standard TGA experiments at different heating rates, we can calculate the activation energy and the pre-exponential factor. The main advantage of MTGA is that it allows the calculation of temperature dependent activation energy without the need for a reaction model $f(\alpha)$ [2]. By assuming that the reacted fraction does not change appreciably during a half-cycle, i.e., the ratio of $f(\alpha_{peak})$ at $d\alpha_{peak}/dt$ and $f(\alpha_{valley})$ at $d\alpha_{valley}/dt$ approaches unity.

$$\frac{d\alpha_{peak}/dt}{d\alpha_{valley}/dt} = \frac{A\exp\left(\frac{-E_a}{RT_{peak}}\right) f(\alpha_{peak})}{A\exp\left(\frac{-E_a}{RT_{valley}}\right) f(\alpha_{valley})} = \exp\left(\frac{-E_a}{R}\left(\frac{1}{T_{peak}} - \frac{1}{T_{valley}}\right)\right) \tag{3.1.5}$$

$$E_a = \left(\frac{RT_{peak}T_{valley}}{T_{peak} - T_{valley}}\right)\ln\left(\frac{d\alpha_{peak}/dt}{d\alpha_{valley}/dt}\right) = \left(\frac{R\left(T^2 - A_T^2\right)}{2A_T}\right)\ln\left(\frac{d\alpha_{peak}/dt}{d\alpha_{valley}/dt}\right) = \frac{RL\left(T^2 - A_T^2\right)}{2A_T} \tag{3.1.6}$$

where, $T_{peak} = T+A_T$ and $T_{valley} = T-A_T$. A new parameter L, defined as the ratio of the maximum and minimum conversion rate in a cycle and is given by:

$$L = \ln\left(\frac{d\alpha_{peak}/dt}{d\alpha_{valley}/dt}\right) \tag{3.1.7}$$

We note here that the activation energy can be calculated as a function of temperature by determining it for many different temperature modulation cycles. However, we still have to determine the order of reaction (reaction mechanism). This can be accomplished by assuming an equivalent rate law (order) for the differential and integral forms of the rate equation. Since we have already obtained the activation energy, the rate law that gives very close values for the pre-exponential factor (A) for both differential and integral forms of the rate equation can be considered as possible reaction mechanism.

For example, for a one-dimensional diffusion reaction model that has been proposed for oxidation of iron by Roy et al. [3]. The differential rate law is $f(\alpha) = (2\alpha)^{-1}$ and the corresponding integral rate law is $g(\alpha) = kt = (\alpha)^2$. The integral law is representative of parabolic kinetics. The following equation shows a straight forward way of

estimating the pre-exponential factor if we assume a one-dimensional diffusion reaction model. Taking logarithm of the differential form of the rate equation (assuming constant E_a):

$$\ln(A) = \ln\left(\frac{d\alpha/dt}{(2\alpha)^{-1}}\right) - \frac{-E_a}{RT} \tag{3.1.8}$$

The reaction rate constant is given by the following expression:

$$k = 2\alpha\beta\frac{d\alpha}{dT} \tag{3.1.9}$$

In the following section, we present the activation energy of samples of Rock Bolts, Splits Sets and Swellex Mn24. The determination of non-isothermal rate law is under progress.

3.1.4. Results of Oxidation Studies

The split sets is a high strength low alloy (HSLA), low carbon steel. The chemical analysis of a representative sample of split sets was done at Laboratory Testing Inc., and the composition is given below in Table No. 2.2. The weight gain plot of split sets, Rock Bolt, and Swellex Mn-24 samples are shown in Figures 3.1.1, 3.1.3, and 3.1.4. It is well known that low carbon steels (and pure iron) form scales consisting of magnetite (Fe_3O_4) and hematite (Fe_2O_3) at low oxidation temperature. The formation of Wustite is not favored thermodynamically (Fe-O equilibrium diagram is shown in Figure 3.1.2). The only characterization of the oxide film formed was performed by Scanning Electron Microscopy (SEM) and further characterization using X-ray Diffraction is necessary to establish the composition of various phases. It is not possible to establish the possible reaction sequence without further characterization. However, visual inspection clearly reveals that the oxidation kinetics is parabolic with a linear region for low oxidation times and a transient region. The activation energy calculated for Swellex Mn-24 is found to be 368 kJ/mol at a temperature of ~750K (476.85^{O}C) and that for Williams Rock Bolt is found to be 341 kJ/mol at a temperature of ~740K (466.85^{O}C).

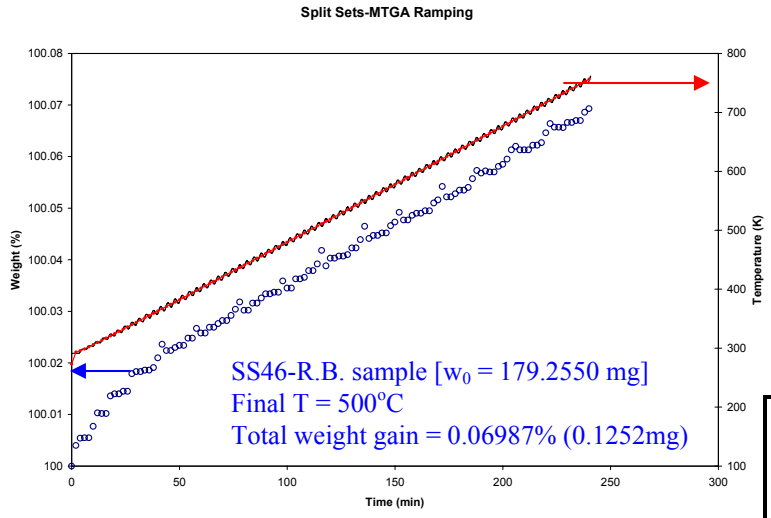

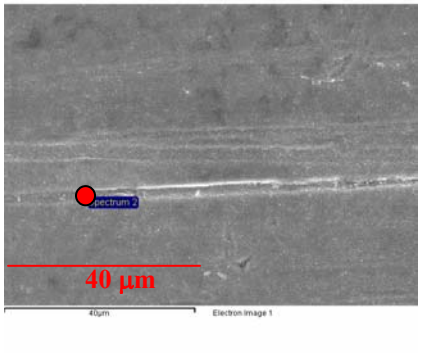

Element	Weight%	Atomic%
O K	14.26	36.31
Al K	1.11	1.67
Si K	0.37	0.54
Mn K	0.71	0.52
Fe K	83.55	60.95
Totals	100.00	

Figure 3.1.1. (a) Weight gain, average temperature and modulated temperature of Split Set rock bolt HSLA sample as a function of time (top left). (b) SEM micrograph of the oxidized surface (top-right) (c) the chemical composition from EDAX. The surface oxide layer appears to be a combination of a-Fe and Fe_3O_4 with smaller oxide content (bottom- right).

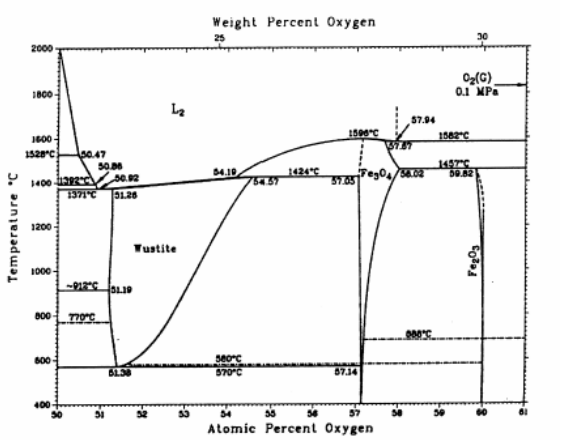

Figure 3.1.2. Binary Fe-O phase diagram. It can be seen that the formation of Wustite is favored (thermodynamically stable) Reference [1].

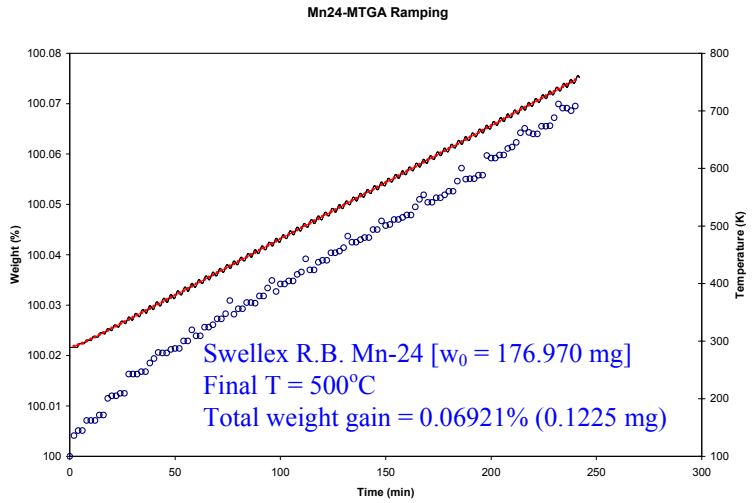

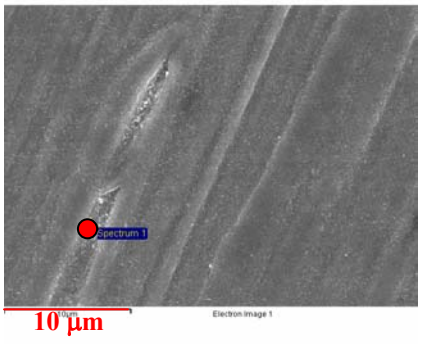

Element	Weight%	Atomic%
O K	17.17	39.76
Al K	7.42	10.19
Mn K	0.84	0.57
Fe K	74.57	49.47
Totals	100.00	

Figure 3.1.3. (a) Weight gain, average temperature and modulated temperature of Swellex Mn-24 sample as a function of time (top-left).
(b) SEM micrograph of the oxidized surface (top-right)
(c) Chemical composition from EDAX. The surface oxide layer appears to be a combination of α-Fe and Fe3O4 with smaller oxide content.(bottom – right)

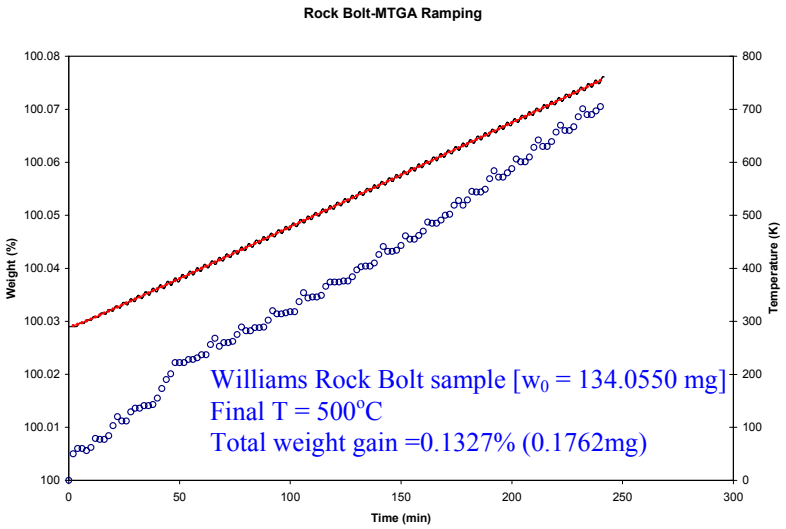

Figure 3.1.4. (a) Weight gain, average temperature and modulated temperature of Rock Bolt sample from YM site as a function of time.

3.1 (a) Characterization of Grain precipitation in Alloy From TGA Samples (Oxidation Studies)

In the last quarterly report we showed that the baseline Alloy 22 exhibited an unusual decrease in mass loss during oxidation of Alloy 22 in oxygen environment in Thermogravimetric analyses (TGA) experiments. At that time we did not know, if there TCP grain boundary or related phases formed during the TGA runs. The experiment involved isothermal oxidation of Alloy 22 at 950°C; initial decreases were observed followed by increases in weight that will be discussed in the following sections. The suggestion of formation of TCP type precipitates were verified by performing scanning electron microscopic analyses on cross sections of the TGA sample followed by electrolytic polishing after the test. These Alloy 22 samples in wrought condition were checked for the presence of TCP phases before the TGA tests, and none were found. Only γ phase structure was observed was observed which was confirmed by X-ray diffraction analyses (already reported in the last quarterly). Also metallographic did not show any precipitates grain boundaries.

We first show samples of the SEM micrograph of the precipitates formed at grain boundaries as well as precipitates within the grains in Figures 3.1.5, 3.16, and 3.1.7. EDS spectra show the compositions of the matrix and certain precipitates are also listed the respective Tables along with the micrographs for particular positions. An example of the grain boundary precipitates formed during oxidation is shown in Figure 3.1.7. X-ray line scans obtained from Ni Kα, Fe Kα, Cr Kα, Mn Kα, W Lα, Co Kα, and O Kα are superimposed on this micrograph to show decreases in Ni and Cr and increase in Mo concentration, and rest of the elements vary very slightly. Figure 3.1.8 shows TGA scans, SEM micrographs, as well EDS spectra and semi quantitative EDS analyses. On the left TGA scans (from the last quarterly report) are shown as reference scans. A SEM micrograph (top right in Figure 3.18) shows the grain boundary precipitates after the completion of the TGA run. Also superimposed in the micrographs are concentrations of the elements, scanned for X-rays obtained from Ni Kα, Fe Kα, Cr Kα, Mn Kα, W Lα, Co Kα, and O Kα Although these are qualitative they show the depletion of Ni and Cr and increase in Mo concentration at the grain boundary. The compositions shown do not fully agree with the TCP phases that are listed in Table 3.1.2. One could suggest that this may be due to oxidation of alloy but these phases were with in the bulk of the samples and oxygen diffusion is slow. On the right hand side of the SEM micrograph an elemental traverse scan (similar to that shown on the micrograph); these clearly show the variation of the elemental composition at the grin boundary. At this time it is difficult to conclude which of the TCP phases are formed during heating of the sample, but these analyses have to be performed using a TEM for accurate determination.

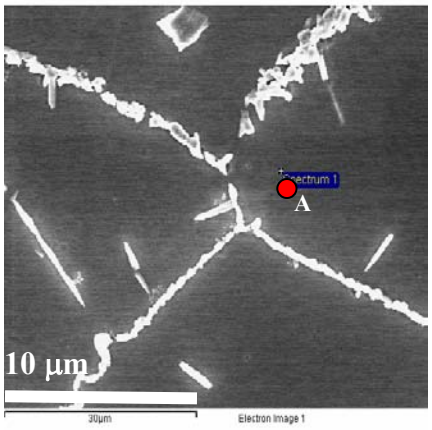

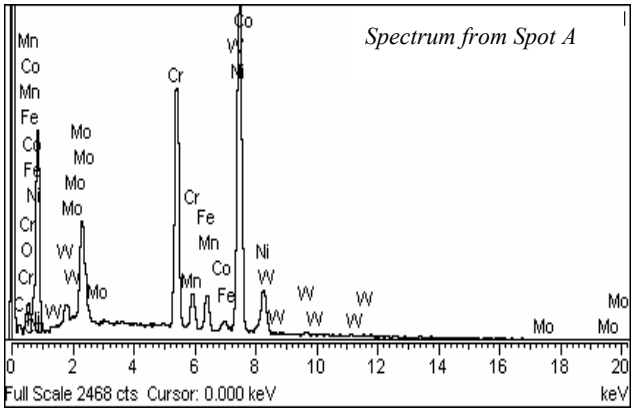

Element	Weight%	Atomic%
C K	3.73	15.59
O K	1.91	6.00
Cr K	20.40	19.71
Mn K	0.62	0.57
Fe K	3.89	3.50
Co K	0.92	0.79
Ni K	56.03	47.96
Mo L	9.82	5.14
W M	2.68	0.73
Totals	100.00	

Figure 3.1.5. SEM micrograph showing grain boundary precipitates in Alloy 22 after the sample was oxidized in a TGA in pure oxygen environment after which it was electrolytically polished before these SEM analyses were performed. THE EDS scan (middle) show presence of matrix elements obtained from the spot (A).

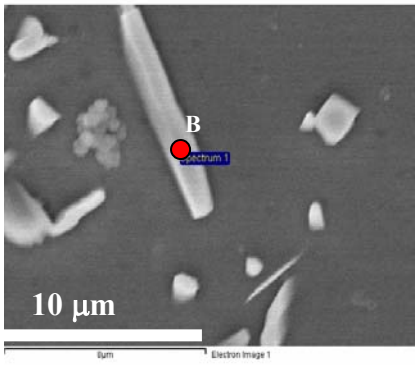

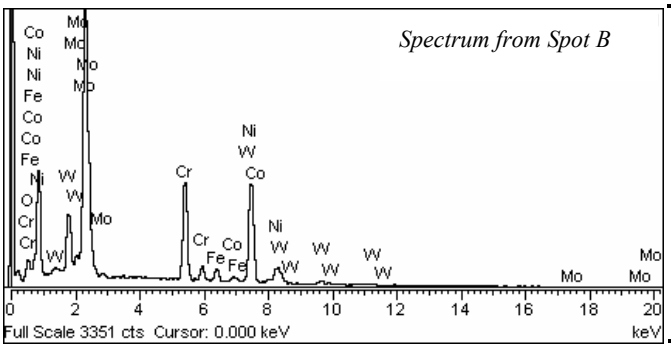

Element	Weight%	Atomic %
O K	3.68	15.20
Cr K	14.21	18.06
Fe K	2.20	2.60
Co K	0.92	1.03
Ni K	27.72	31.20
Mo L	40.94	28.20
W M	10.33	3.71
Totals	100.00	

Figure 3.1.6. SEM micrograph precipitates in Alloy 22 within the grain after the sample was oxidized in a TGA in pure oxygen environment after which it was electrolytically polished electrolytically polished.

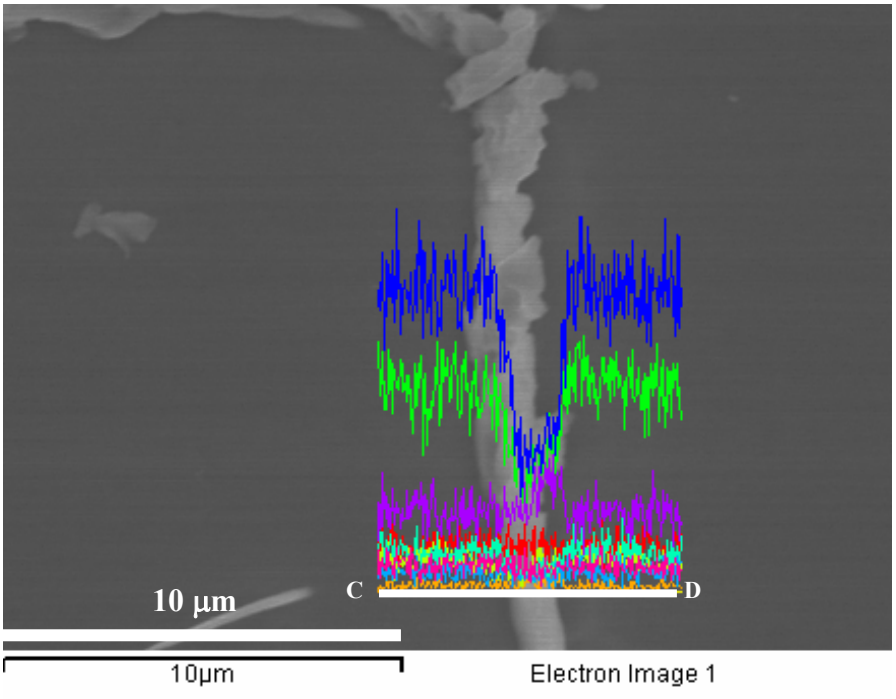

Figure 3.1.7 SEM micrograph precipitates in Alloy 22 showing variation of composition in the grain boundary after the sample was oxidized in a TGA in pure oxygen environment. There is a decrease in Ni content and increase of Mo concentration. Please note that a larger sample of size (mm diameter and mm thickness was used) for these tests such that X-ray diffraction characterization as well as scanning electron microscopic characterization may be performed. (Same sample as above)

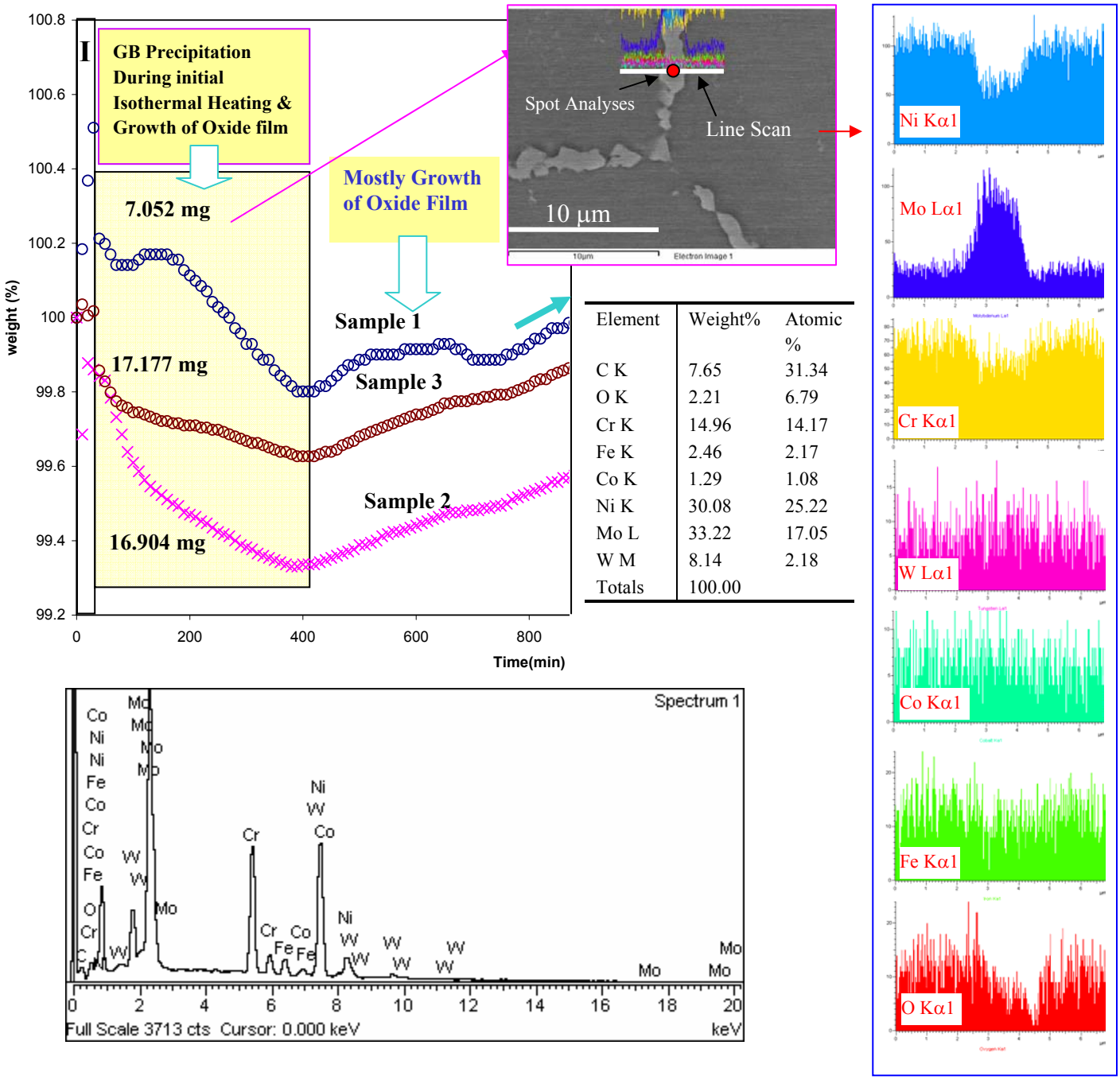

Element	Weight%	Atomic %
C K	7.65	31.34
O K	2.21	6.79
Cr K	14.96	14.17
Fe K	2.46	2.17
Co K	1.29	1.08
Ni K	30.08	25.22
Mo L	33.22	17.05
W M	8.14	2.18
Totals	100.00	

Figure 3.1.8. Example of initial weight loss during isothermal oxidation (in the shaded region marked II). This is due larger volume (lower density) grain boundary and other TCP precipitates formed during isothermal oxidation of Alloy 22 in Pure O_2 atmosphere @ 980°C, using a TGA is due to the formation of grain boundary and other TCP type phases.

Table 3.1.2. Structure And Lattice Parameters of Alloy 22 (γ -Phase), Grain Boundary Precipitates and oxides formed during Heating *[Ref. D. D. Gorhe, MS Thesis, UNR August* 2004 and Cieslak et al. LLNL*]*.

Type	Phases	Hastalloy - Alloy 22 Composition (Weight %)						
		Cell Volume nm^3	Ni	Cr	Mo	W	Fe	Co
Alloy	γ Cubic (FCC)	0.0470	58.5	21.6	12.7	2.9	3.4	0.9
Grain Boundary Precipitates (TCP Phases)	μ Hexagonal	0.5088	33.1	19.3	38.7	6.3	2.1	0.6
	σ Tetragonal	0.3920	34.5	23.4	34.9	4.2	2.2	0.9
	P Orthorhombic	0.7315	32.6	21.7	37.4	5.3	2.2	0.9

To summarize the Thermogravimetric studies on c*arbon and Low Alloy Steels Rock Bolts (Non Isothermal studies)* show comparable weight gain in Williams (MCS) and Split Set (HSLA) rock bolts, ranging between 0.06 to 0.08 wt.% in the temperature range of 50 to 500^{o}C. *Base line for Alloy 22 (Isothermal studies)* showed an initial weight loss due to GB precipitate formation - higher unit cell volumes and lower densities. When GB precipitate formation is complete then oxide formation becomes predominant. Cr_2O_3 and $NiCrO_3$ form (From XRD/SEM results). Weight gain is due to increase in density of oxides relative to the parent alloy.

References for Section 3.1.

1. T.P. Bagchi, P.K. Sen, Thermochimica Acta 51 (1981) 175-189.
2. R.L. Blaine, B.K. Hahn, Journal of Thermal Analysis and Calorimetry 54 (1998) 695–704.
3. S.K. Roy, A. Auddya, S.K. Bose, Reactivity of Solids 6 (1989) 301-320.
4. H. A. Wriedt, in *Binary Alloy Phase Diagrams*, 2nd edn., Vol. 2, T. B. Massalski, H. Okamoto, P. R. Subramanian, and L. Kacprzak, eds. (ASM Intern., Metals Park, OH, 1990), pp.1739–1744.

3.2 Task No. 2 - Electrochemical Behavior of Swellex Rock Bolt (In inflated State)

3.2.1 Introduction

Swellex Rock Bolt is one of the Friction Rock Stabilizers [FRS} commonly used as tunnel support. Swellex Rock Bolts are High Strength Low Alloy (HSLA) steels [1]. These steels have better mechanical properties than as rolled carbon steels, largely by virtue of grain refining and precipitation hardening. Due to the superior mechanical properties of HSLA steels, they allow more efficient designs with improved performance, reductions in manufacturing costs and component weight reduction to be produced. Applications include under ground tunneling support, oil and gas pipelines, automotive sub-frames, offshore structures and shipbuilding. Those steels provide strength-to-weight ratios over conventional low-carbon steels.

Typically, HSLA steels are low-carbon steels (0,06% to 0,12%) with 004% to 2.5% Manganese, strengthened by small additions of elements, such as columbium, copper, vanadium or titanium and sometimes by special rolling and cooling techniques. Elements such as copper, silicon, nickel, chromium, and phosphorus can improve atmospheric corrosion resistance of these alloys with e an associated cost penalty. Chemical analyses performed LTI are shown in the materials section.

3.2.2 Experimental Procedure

Electrochemical potentiodynamic tests were performed by using the same setup which was used for the Alloy-22 according to the Implementing Procedure (IPR-18)[2] Electrochemical Corrosion Testing and ASTM G-5[3] Procedures.

Swellex Mn24 rock bolt (in expanded or inflated state) were cut mounted and the working electrodes were mounted in epoxy with the 0.949 cm^2 bottom surface area and at the other end copper wire is exposed for the electrical connection as shown in the figure 3.2.1.

The experimental procedure was followed was similar to that of Alloy-22 with the scanning rate of 0.2mV/sec and Potential sweep from -1V to 0V. The tests were performed using deaerated (nitrogenated) or aerated (oxygenated) conditions using 150 ml/min flow rates. The gas flow was started approximately one hour before the start of the experiment which was enough to get the constant corrosion potential for these type of Rock Bolts.

Figure 3.2.1 Swellex sample mounted for electrochemical tests.

Two sets of experimental conditions were followed:

1. Polarization experiments of Swellex Mn24 Rock bolt in different concentrations (1X, 10X, and 100X) at 25^oC in de-aerated (Nitrogen) Yucca Mountain Water.
2. Polarization experiments of Swellex Mn24 Rock bolt in different concentrations (1X, 10X, and 100X) at 25^oC in aerated (Oxygen) Yucca Mountain Water.

Table 3.2.1. Yucca Mountain (YM) Water Chemistry for different concentrations

Chemicals	1x YM (mg/L)	10x YM (mg/L)	100x YM (mg/L)
$MgSO_4.7H_2O$	50	500	5000
$MgCl_2.6H_2O$	100	1000	10000
$CaCl_2.2H_2O$	196	1960	19600
$CaSO_4.2H_2O$	210	2100	21000
$KHCO_3$	50	500	5000
$NaHCO_3$	200	2000	20000
$NaSiO_3.9H_2O$	210	2100	21000
NaF	2	20	200

The corrosion rate is calculated by using the following equation (ASTM G102) [4]:

$$CR = \frac{EW.K.I_{corr}}{\rho} \mu m / year \qquad (3.2.1)$$

Where, K = 3.27×10^{6} µm.g/A.cm.year
EW = Equivalent weight = 27.24 (for Swellex Mn24 Rock Bolt)
ρ = density =7.858 g/cm^3

3.2.3 Results and Discussion

A. Polarization Experiments at room temperature and Under Deaerated conditions for 1x,10x,and 100x YM water concentrations

Polarization experiments of Swellex Mn24 Rock bolt in de-aerated (Nitrogen) 1X Yucca Mountain Water chemistry at 25°c temperature. Using the equation No. 3.2.1 the corrosion rates (CR) were calculated from the data shown in Figures 3.2.2 (a and b); which tests performed to show reproducibility of these data. The CR were 8.5 and 9.05 mm/yr, which appear to be reasonably close.
In a similar manner potentiodynamic tests were performed on the Swellex Mn-24 sample using 10x, 100x YM concentrations and the polarization curves with corrosion rates are shown in Figures 3.2.3, and 3.2.4.

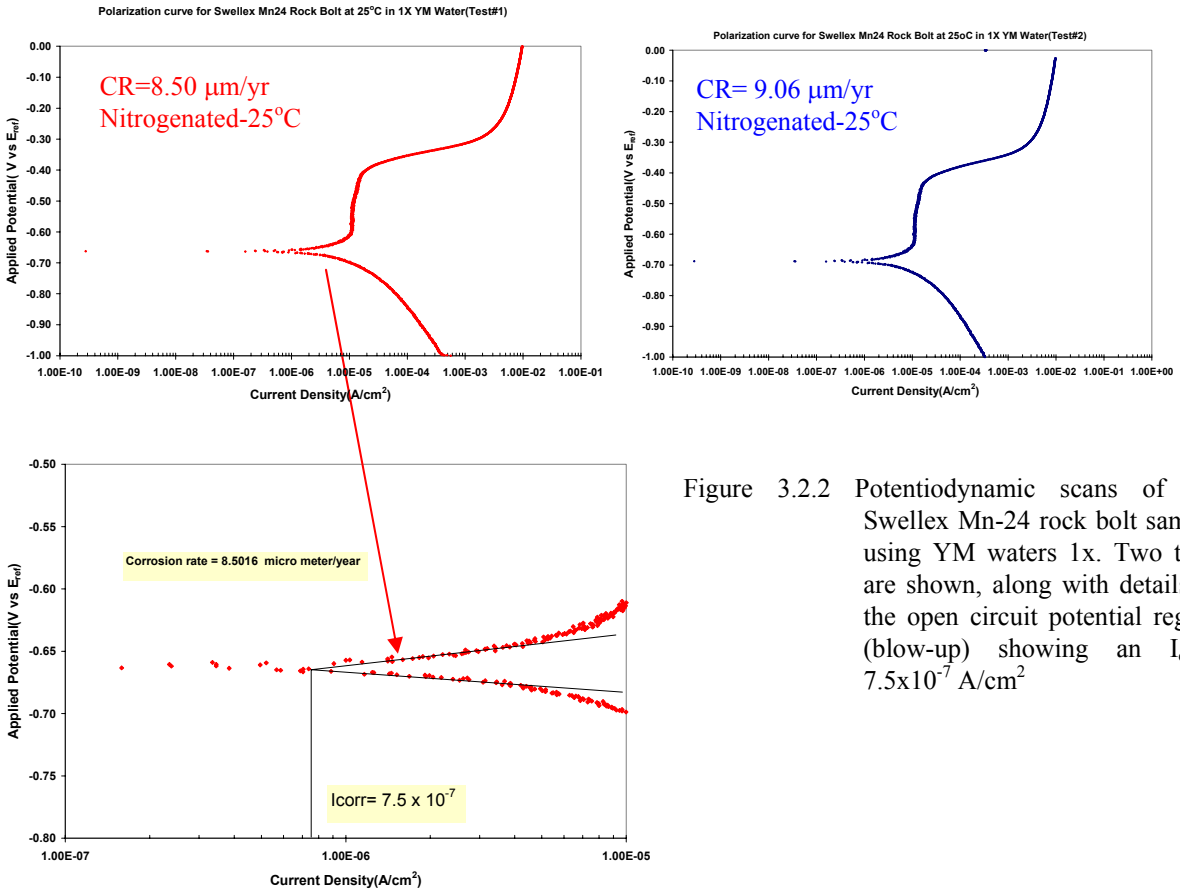

Figure 3.2.2 Potentiodynamic scans of the Swellex Mn-24 rock bolt sample using YM waters 1x. Two tests are shown, along with details of the open circuit potential region (blow-up) showing an I_{corr}= $7.5x10^{-7}$ A/cm^2

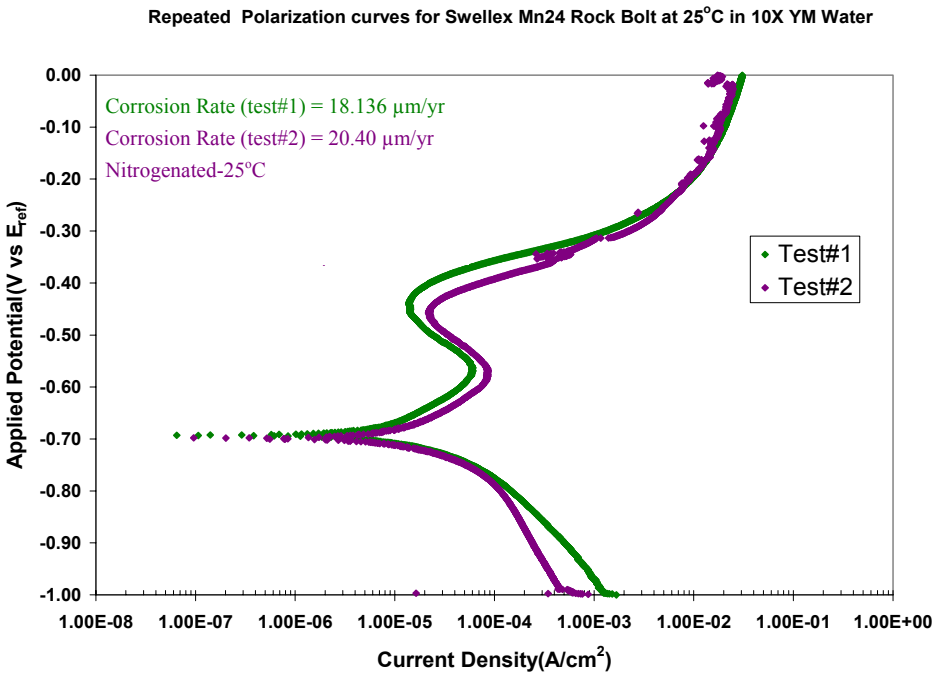

Figure 3.2.3. Polarization curves Swellex Mn24 Rock bolt in de-aerated (Nitrogen) 10X Yucca Mountain Water chemistry at 25°C temperature.

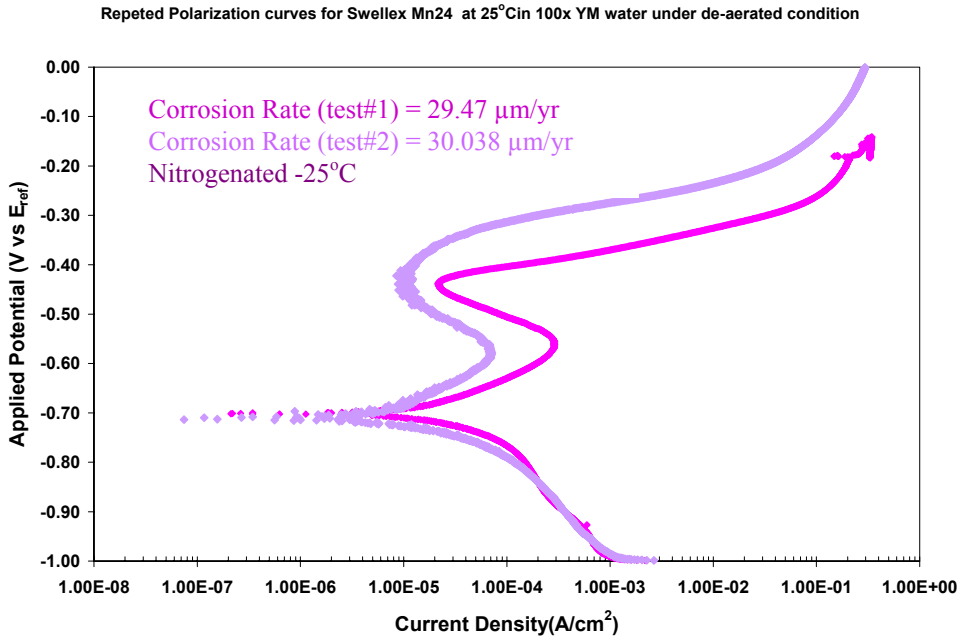

Figure 3.2.4. Polarization curves Swellex Mn24 Rock bolt in de-aerated (Nitrogen) 100X Yucca Mountain Water chemistry at 25°C temperature.

The corrosion rates for the Swellex Mn-24 in deaerated conditions measured form the potentiodynamic curves are listed in table 3.3.1. These CR's are reasonable for this type of steel for the YM waters used in this study. These CR's are plotted in Figure 3.2.5 which show a significant increase in the CR as a function of YM water concentration, due to increased of ionic concentration in the YM waters

Table 3.2.2. Tabulation of Corrosion rates of Swellex Mn-24 rock bolts in deaerated conditions.

YM water Concentration	*Swellex Rock Bolt Mn 24 Corrosion Rate (µmpy)*		
1X	Test#1	Test#2	Average
	8.50	9.06	8.78
10X	Test#1	Test#2	Average
	18.136	20.40	19.268
100X	Test#1	Test#2	Average
	29.47	30.606	30.038

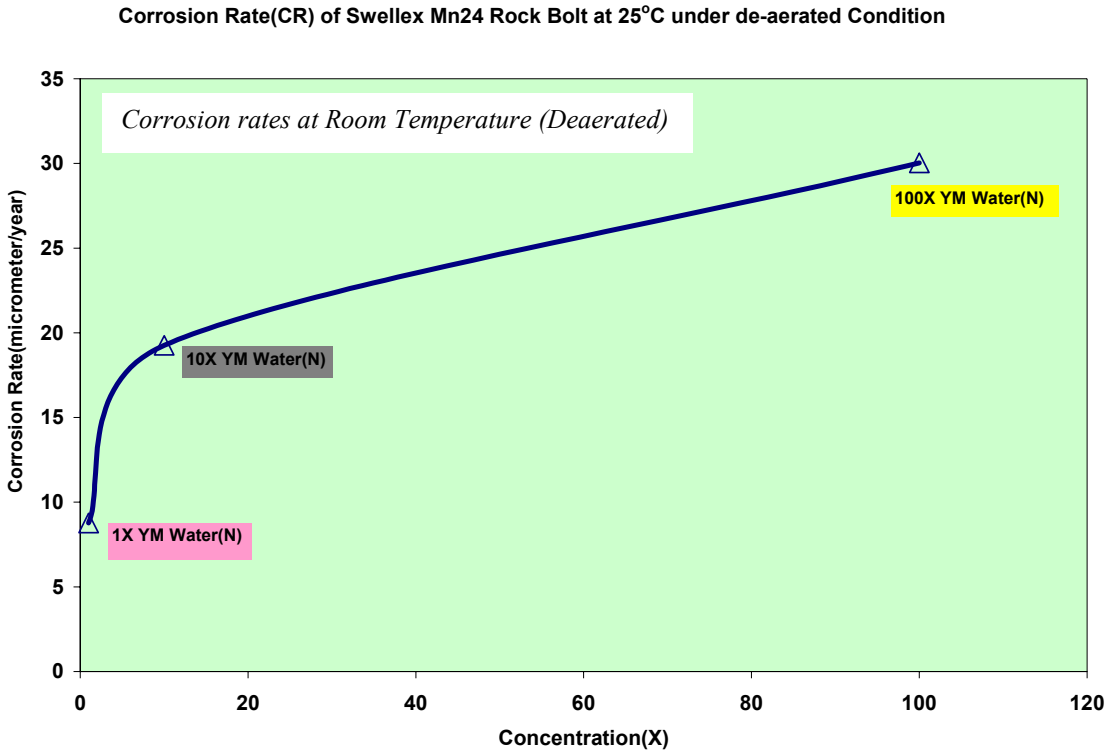

Figure 3.2.5 Summary of the corrosion rates of Swellex Mn-24 rock bolts form the Polarization curves in de-aerated (Nitrogen)1x, 10x, and 100X Yucca Mountain Water chemistry at 25°C. The CR's range from 9 to 30 µm/yr in de-aerated condition at room temperature.

Anodic polarization curve for a metal which shows general passive behavior taken from Prof. Denny Jones Text book of "Corrosion" is shown in Figure 3.3.6 which shows passivation 10x and 100x YM water concentrations based on the corrosion potential. As expected there is no transpassive region observed because the upper limit of applied potential is 0V. Microscopical characterization of the sample after the experiments showed formation of pits due to the passive layer breakdown in 100X concentrated YM water under de-aerated condition. These pits were also observed in 10 x YM water concentration samples, possibly due to the breakdown of oxide layer formed in anodic region.

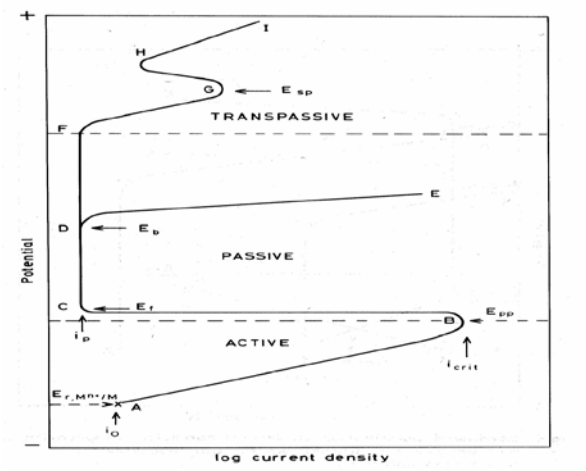

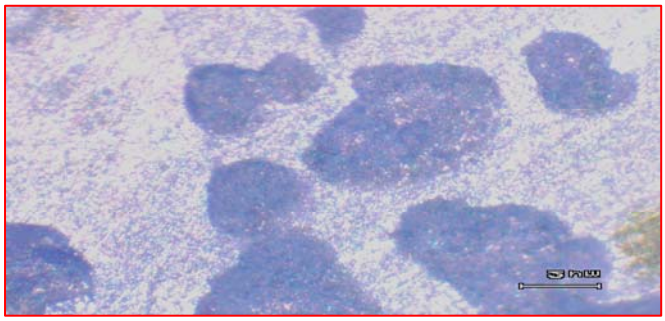

Figure 3.2.6(left) A typical potential vs. current curve taken form a Prof. Denny Jones text book.
Figure 3.2.7(right) Optical micrograph (100x) taken form the sample after the polarization test at room temperature in nitrogenated conditions (100x YM waters).

B. Polarization Experiments at room temperature and Under Oxygenated aerated conditions for 1x,10x,and 100x YM water concentrations

Polarization curves of the Swellex Mn24 Rock bolts obtained in aerated (oxygenated) condition with 1x, 10x, and 100x Yucca Mountain Water chemistry at 25°C and the data obtained are shown in Figure 3.2.8. In aerated conditions (upper limit), the CR's increase more significantly than those observed in nitrogenated condition, as expected, with the increase in the concentration of electrolyte. The I_{corr} and CR were calculated form the data and are shown in Table 3.2.2. It should be noted that the E_{corr} for all nitrogenated experiments were approximately -0.7V which is near to the corrosion potential of Iron (Fe).

In the case of aerated experiments the E_{corr} values were different for 1x, 10x, and 100x YM waters. From the combined plot (Figure 3.2.5), the E_{corr} for 1x is approximately -0.3V, is possibly due to the higher potential of oxygen in cathodic reaction. The E_{corr} for 10x ~ -0.6V may be due to the formation of Fe oxide films, which is near to the corrosion potential of Fe. For the 100x E_{corr} is little higher than the 10x, may be due to the increased concentration of ions in electrolyte such as Cl^- and SO_4^-, where there is a possibility of reformation of layers that leads to higher corrosion potential. From the Figure 3.2.8 and the Table 3.2.3, it can be concluded the corrosion rate(CR) is increased dramatically for the aerated experiments as compared to de-aerated experiments. The CR's for Swellex Mn24 Rock Bolts are higher when compared with the MCS (Medium Carbon Steels) Rock Bolts [5].

Table 3.2.3. Corrosion rates of Swellex Mn24 rock bolts (1x, 10x, and 100x) obtained at room temperature and under oxygenated conditions.

Concentration	Corrosion Rate(μm/yr) Aerated (Oxygenated Condition)	I_{corr} (A/cm^2)
1X	136.8	1.2×10^{-5}
10X	453.4	4×10^{-5}
100X	1360.26	1.2×10^{-4}

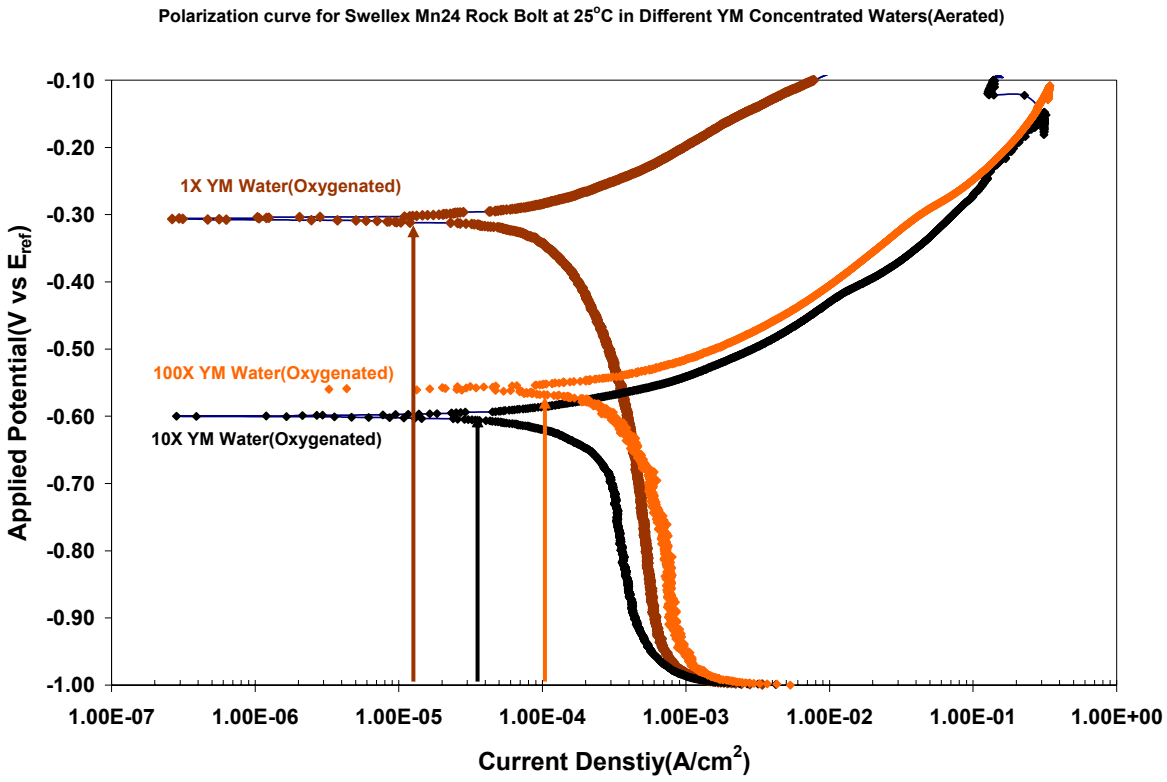

Figure 3.2.8 Potentiodynamic scans of Swellex Mn-24 rock bolts in inflated state at room temperature under aerated (oxygenated) and deaerated (nitrogenated) environments (YM waters, 1x,10x, 100x concentrations).

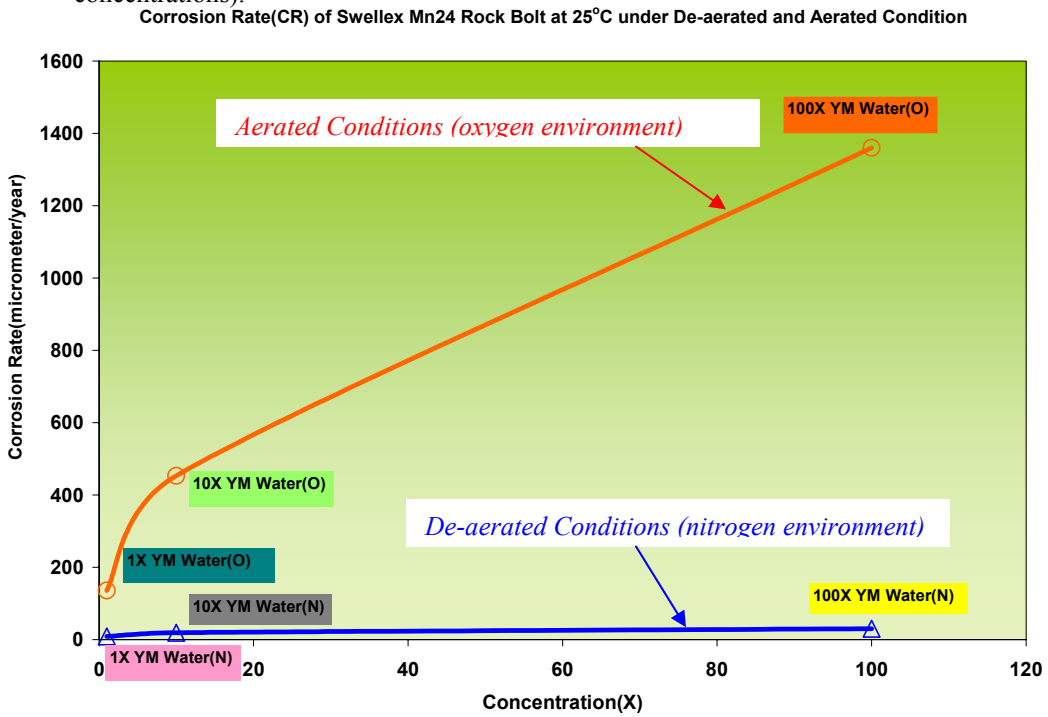

Figure 3.2.9. Summary of the corrosion rates of Swellex Mn-24 rock bolts from the Polarization curves in de-aerated (Nitrogen) and aerated conditions (1x, 10x, and 100x Yucca Mountain Water chemistry).

Table 3.2.3. Corrosion rates of Swellex Mn-24 Rock bolts under aerated and non aerated conditions For the 1x, 10x, 100x YM water chemistry.

YM Water Concentration	Corrosion Rate(µm/yr) De-aerated (Nitrogen)	Corrosion Rate(µm/yr) Aerated (Oxygen)
1X	8.78	136.8
10X	19.268	453.4
100X	30.038	1360.26

References for Section 3.2. (Swellex rock bolt Electrochemical Studies)

1. J.Ranasooriya,"Corrosion of friction rock stabilizer-experience from western Australia" Proceedings of ROCKSITE-99, Bangalore, India.
2. ASTM G-5 , " Standard Refrence Test Method for Making Potentiostatic and Potentiodynamic Anodic Polarization Measurements",Annual Book of ASTM Standards, Vol 03.02.
3. http://hrcweb.nevada.edu/qa/IPR/IPR-018R3.pdf
4. ASTM G102, "Standard Practice for Calculation of Corrosion Rates and Related Information from Electrochemical Measurements", Annual Book of ASTM Standards, Vol 03.02
5. A.Yilmaz, "Degradation and Failure susceptibility of carbon steels in simulated yucca mountain nuclear repository environments", Dissertation, UNR-2003.

3.3. Task No. 5 -- Hydrogen Permeation Experiments and Diffusion Rates of Williams Rock Bolts

3.3.1. Background

Hydrogen permeation and trapping sites are of significance to embrittlement of steels; these characteristics were properties were determined in this period. William rock bolts from YM site (Specimen RB-001) was used for these studies as these rock bolts have been electrochemically fully characterized in the last project. A Devanathan and Stachurski's electrochemical permeation method was used to determine these properties. The above method has been widely used to calculate the diffusivity and also to classify the role of traps and their effect on hydrogen diffusivity. In general, trapping sites may be reversible or irreversible depending on their binding energies of the atoms. The contribution of traps on the diffusivity can be obtained by successive permeation transients on the same sample. Usually, during the first permeation transient, all the reversible and irreversible traps are filled and during the second permeation transient, irreversible traps are ineffective and only reversible and lattice sites are active and affect the diffusivity. Hydrogen permeation studies are performed on flat and thin specimens by electrochemical charging with hydrogen [1-3].

The hydrogen permeation rate ($J_\infty L$) (mol H cm^{-1} s^{-1}), effective diffusivity (D_{eff}) (cm^2 s^{-1}) and solubility (C_o) (ppm) were calculated using the following equations[1]:

Analysis of Hydrogen Permeation Rate ($J_\infty L$) (mol H cm^{-1} s^{-1})

$$J_\infty L = \frac{Ip_\infty L}{nF} \tag{3.3.1}$$

Where J_∞ is the steady-state flux, L is the specimen thickness in (cm), Ip_∞ is the steady- state permeation current density in A/cm^2, "n" is the number of electrons transferred, F is the Faraday's constant (96485 Coulombs/mol.) and L is the specimen thickness.

Analysis of effective diffusivity (D_{eff}) (cm^2 s^{-1})

The steady state hydrogen permeation flux (J_{ss}) is given as

$$J_{ss} = \frac{I_{ss}/A}{F} = \frac{D_l C_0}{L} \tag{3.3.2}$$

Where, I_{ss} = steady state atomic hydrogen permeation current (μA),
A = Exposed area of specimen in the oxidation cell (cm^2),
C_0 = Sub-surface concentration of atomic hydrogen at the charging side of the specimen (mol/cm^3)
D_l = Lattice Diffusion Coefficient of Atomic hydrogen (cm^2/s)
The effective Diffusion Coefficient can be calculated based on the elapsed time (t_{lag}) at $J(t)/J_{ss} = 0.63$,

$$D_{eff} = \frac{L^2}{6t_L} \tag{3.3.3}$$

Where t_L is the lag time at $J(t)/J_{ss} = 0.63$ and L is the thickness of the specimen (cm)

3.3.2. Experimental

Hydrogen permeation experiments were performed in a system with two compartments separated by carbon steel membrane as introduced by Devanathan-Stachursky. Hydrogen was charged galvanostatically at an applied cathodic current density of $1mA/cm^2$ and the anodic side of the specimen was fixed at a potential of + 0.28 V with respect to Silver-Silver Chloride (Ag-AgCl) to enable the oxidation of atomic hydrogen that diffused through the steel membrane. The electrolyte on the charging and the oxidation sides of the cell was de-aerated 0.1N NaOH. De-aeration was done by purging N_2 gas for one hour prior to the experiment and was continued until the end of the experiments. The anodic side of the membrane was electroplated with Ni to avoid corrosion. To enhance the hydrogen absorption, 10mg of arsenic trioxide (As_2O_3) was added in the charging cell as a hydrogen recombination poison. Effect of trapping was investigated by recording a second permeation transient immediately after the first transient.

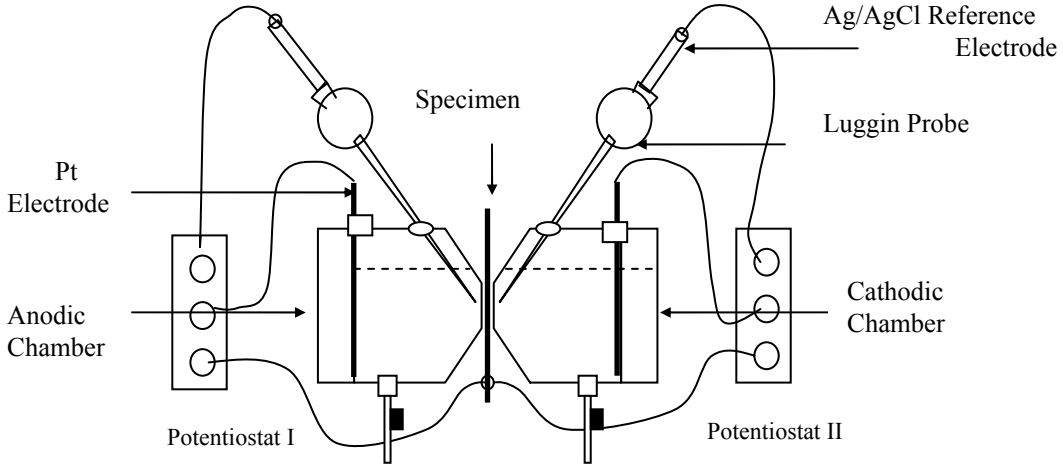

Figure 3.3.1. Schematic of Devanathan-Staruchi cell showing the two compartments for permeation of hydrogen. This experiment requires two potentiostats.

Figure 3.3.2. William M.C. Rock Bolt (left). Sample coupons machined form the rock bolt shown of three different thicknesses indicated above for the permeation tests (right).

3.3.3. Results

Current vs. time data was collected for each thickness on the potentiostat and is displayed in Figure 3. The current, as seen in equation (2) is directly related to the flux, so the general trends can be seen in this data. There are two separate transients collected on each set by using two cathodic charging periods. All data sets showed a more reliable steady state during the second cathodic charging period, as well as occasionally different shapes in the transient curves as they approached steady state. This occurs because all hydrogen trapping sites, reversible and irreversible are filled during the first charging period, while only the reversible traps are filled during the second charging period. [1,3]

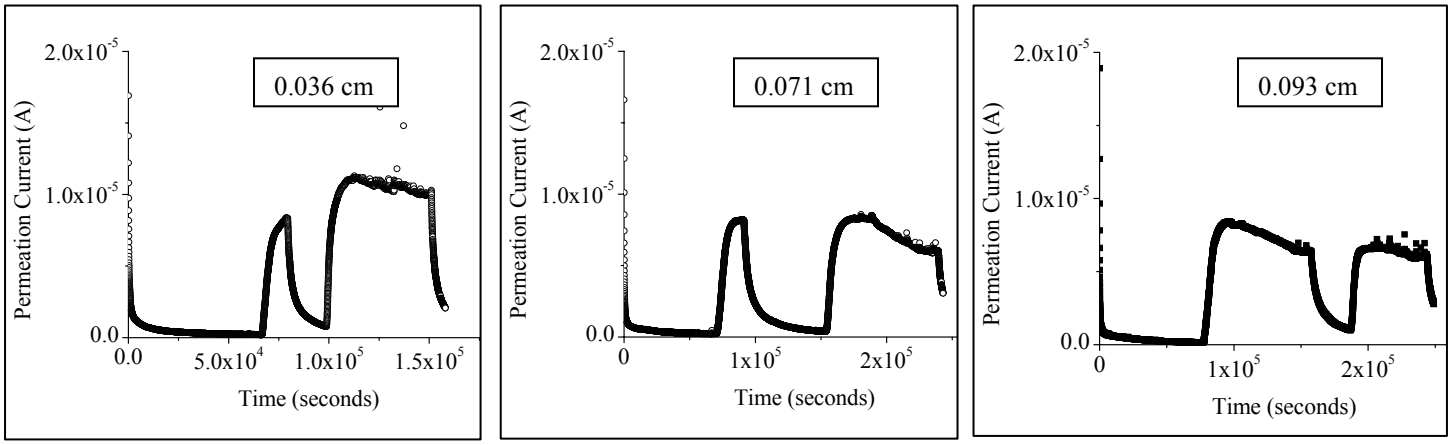

Figure 3.3.3. Permeation current as a function of time on rock bolts with thicknesses of 0.036 cm (left), 0.071 cm (middle) and 0.093 cm (right).

The steady state current was determined from the graph, with the steady state flux being calculated using equation (3.3.2). The result of this is displayed in Table 3.3.1 below. The steady state flux was then plotted vs. reciprocal thickness as shown in Figure 3.3.4. The linear nature of the data shown helps to confirm that hydrogen transport occurred through bulk diffusion.

The flux is also calculated at each point and each run is compared by displaying the start of cathodic charging as the initial time for each run. This is displayed for both the first and second cathodic charging in Figure 5. The second transient in particular shows that the steady state flux decreases with increasing thickness. As long as the effective diffusivity and the concentration of hydrogen on the cathodic charging side remain constant the change in flux should come exclusively from the change in thickness, with the plot in Figure 3.3.4 helping to verify this.[1] When compared to results from other materials this should also be related to how well the material can withstand hydrogen uptake, as the more flux that occurs the more likely hydrogen induced cracking will occur.[4,5]

Notice that there are some occurrences of spikes in the flux, especially in the second transients. These are most likely the result of either void formations within the material, or a break in the surface layer of the material.[1] This also serves to verify the previous statement that cracking is more likely to occur when the flux is higher, as the spikes in the flux have much greater magnitude in the higher flux 0.036 cm thickness.

The lag time (time where J/Jss = 0.63) was obtained for each thickness and used with equation (3.3.3) to calculate the effective diffusivity (D_{eff}). The results of this calculation are displayed in Table 1. This calculation relies on the assumption that trapping only occurs at steady state, so that the hydrogen being released during the upward slope is only diffusing hydrogen. This has been assumption has been verified in literature. [6]

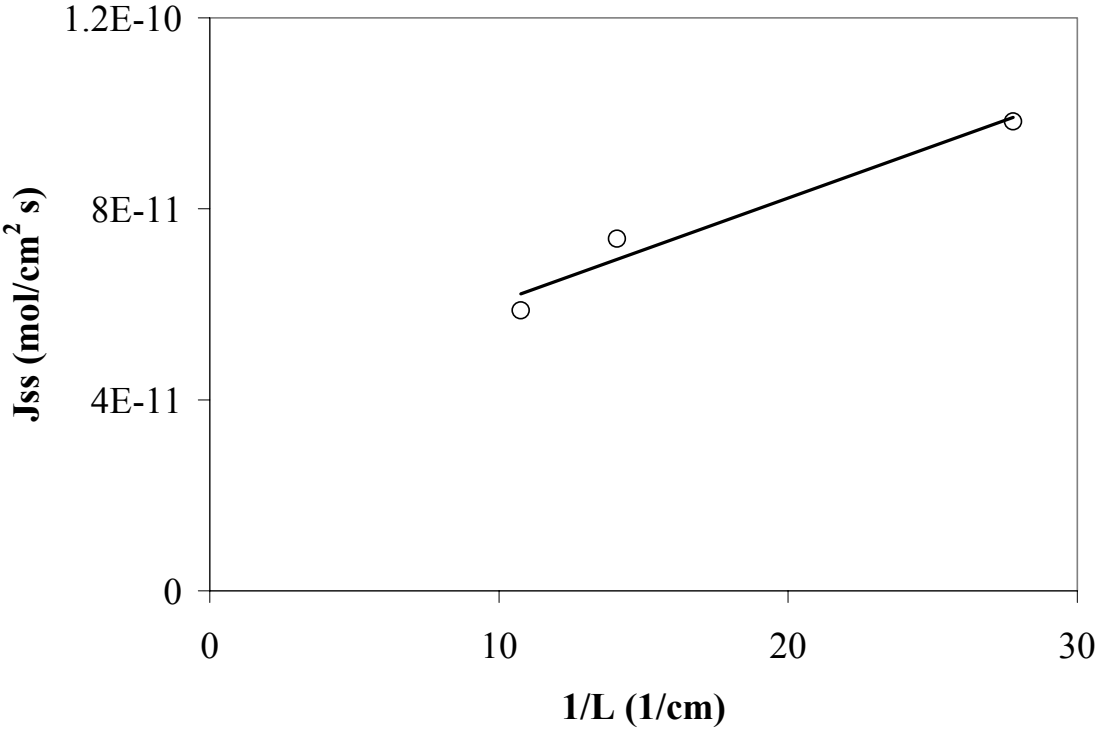

Figure 3.3.4. Steady state flux (Jss) vs. 1/L

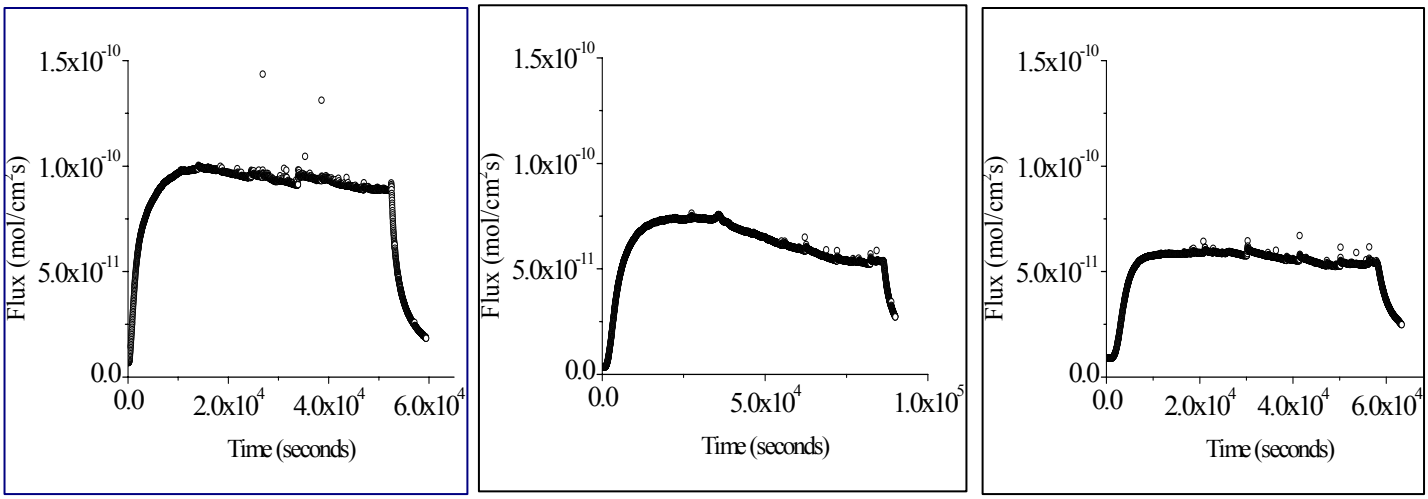

Figure 3.3.5. Transients from first cathodic charging on rock bolts with thicknesses of 0.036 cm (left), 0.071 cm (middle) and 0.093 cm (right)

Table 3.3.1 Hydrogen Diffusion Coefficients of Williams Rock Steel from YM site (medium carbon steel)

Rock bolt (Medium Carbon Steel) results				
Test	L (cm)	Jss (mol/cm^{2}s)	Deff (cm^2/s)	Source
1	0.036	9.83E-11	1.02E-07	Notebook UCCSN-UNR-072 vol 1. pp 12
2	0.071	7.37E-11	1.55E-07	Notebook UCCSN-UNR-072 vol 1. pp 16
3	0.093	5.87E-11	1.99E-07	Notebook UCCSN-UNR-072 vol 1. pp 14

As can be seen the effective diffusivities, which should have similar values, show relatively good relation to each other. The steady state flux shows proper trending downward with increased thickness. There does appear to be some changes in diffusivity with thickness, which may be due to the surface effects having a small impact at lower thicknesses.
Although this sample is representative of rock bolts currently in place at the site, other materials, such as stainless steels, are being considered as potential materials to use for rock bolts. Because of this, other materials will also be studied in this manner to compare the hydrogen susceptibility of various potential materials. This will provide a set of data useful to those making decisions on which materials to use for structural emplacements such as rock bolts.

References forSection 3.3. (Hydrogen permeation Williams Rock Bolts)

1. ASTM G148 Standard Practice for Evaluation of Hydrogen Uptake, Permeation and Transport in Metals by an Electrochemical Technique, p724
2. M.A. V. Devanathan and Z. Stachurski, Proceedings of Royal Society, A270, (1962), p90.
3. A. Turnbull and D.H. Ferriss, NPL Report DMA (D) (1988), p162
4. G.M. Pressouyre, R. Blondeau, G. Primon and L. Cadiou (eds. C.G. Interrante and G.M. Pressouyre)- Proceedings of the First International Conference on Current Solutions to Hydrogen Problems in Steels, 1982, Washington, D.C., p.212.
5. G.M. Pressouyre, R. Blondeau, G. Primon and L. Cadiou, (eds C.G. Interrante and G.M. Pressouyre)- Proceedings of the First International Conference on Current Solutions to Hydrogen Problems in Steels, ASM, Washington, D.C., p.18 (1982).
6. L. Coudreuse and J. Charles, Corrosion Sci., 27 (1987), p.1169.

3.4. Electrochemical and Stress Corrosion Studies on Baseline material (Alloy 22)

3.4.1. Introduction and Background

Corrosion rate was determined by using electrochemical methods for Alloy 22 at different temperature in the simulated YM water. Potentiodynamic and EIS tests were run to determine the corrosion rate. A Gamry potetiostat was used for this electrochemical test. In electrochemical studies, a metal sample with a surface area of a few square centimeters is immersed in a solution typical of the metal's environment in the system being studied. Additional electrodes are immersed in the solution, and all the electrodes are connected to a device called a potentiostat. A potentiostat allows changing the potential of the metal sample in a controlled manner and measuring the current that flows as a function of potential. From the plot of current (in log scale) vs. voltage we can determined the corrosion current (I_{corr}) and Corrosion potential (E_{corr}). The corrosion rate can be calculated using the equation given in Section 3.2.2.

3.4.2. Experimental

Electrochemical tests were performed in a one-liter flask of Pyrex brand glass, shown with the set-up of electrochemical experiments in Figure 3.4.1. A disk shape lid constructed out of 2 cm thick Teflon to seal the cell by means of o-ring, was held in place by compression clamps. A tapered Teflon plug with two holes was machined for the middle opening of the lid, in which cylindrical receptacles for specimen and a Luggin probe were placed as shown in the figure. Several other receptacles on the lid sealed the entire cell elements via threaded o-ring fittings. The tapered Teflon stopper constructed for the larger central hole of the lid held both the specimen and Luggin probe in close proximity, as shown in the figure. Cylindrically shaped working electrodes (test specimens) were

mounted in epoxy with their 1 cm^2 bottom surface area and electrical connection wire exposed out of it, as shown in Figure 2. A large (~10 cm^2) platinum sheet sealed to a glass capillary was used as a counter electrode to provide good conductivity in the electrolyte. The Luggin probe tip and Ag/AgCl reference electrode were connected via the test solution (YM water) in the probe, without using a salt bridge. Continuously purged gas (nitrogen or oxygen) in the sealed cell maintained constant pressure above the solution, and formed a tall column (8-10cm) of solution bridge inside the probe, which connected the Luggin tip and the reference electrode. Therefore, the reference electrode was able to be placed well above the solution level, outside the cell. Thus, the set-up avoided excessive heat on the reference electrode, by means of the temperature gradient created along the solution bridge in the probe. All the tests for Alloy 22 reported in this report were performed in de-aerated water (nitrogen purging).

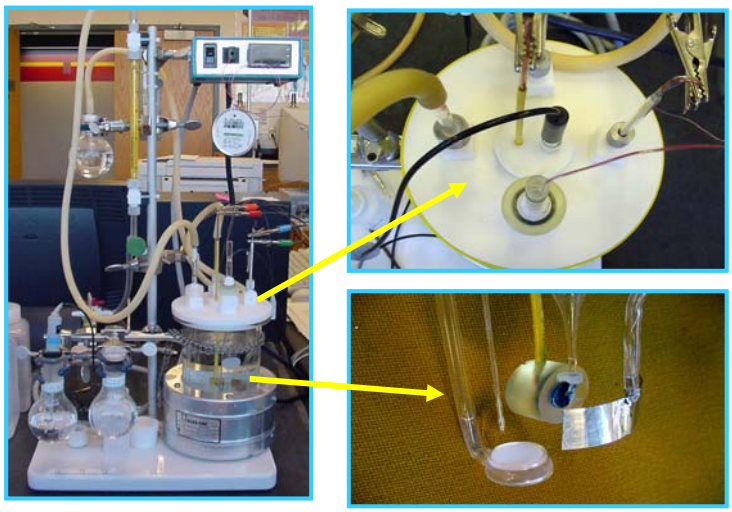

Figure 3.4.1. Cell design for electrochemical tests

Figure 3.4.2 Epoxy mounted specimens for linear polarization tests and impedance Spectroscopy

Details of experimental procedures for have already been outlined in the last quarterly report, and the electrolyte composition used is given in Table 3.4.1.

Table 3.4.1. Yucca Mountain Water chemical composition; pH:7,5

Ions	Na^+	SiO_2	Ca^{2+}	K^+	Mg^{2+}	$HCO3^-$	Cl^-	$SO4^{2-}$	F^-
Mg/l	61.3	70.5	101	8.0	17.0	200	117	116	0.86

3.4.3. Results

Preliminary results of Polarization curves for Alloy 22 at different temperatures are shown in figure 3. All the tests were run in 100x simulated YM water under de-aerated conditions. The corresponding EIS scan is also presented to the left side of polarization curves. At room temperature and 85° C there is a re-passive region in the curves. This re-passivation occurs between 0.40 V to 0.80 V. For other temperatures it doesn't show any re-passivation. The corrosion potential (E_{corr}) for all the temperature is around 0.75 V.

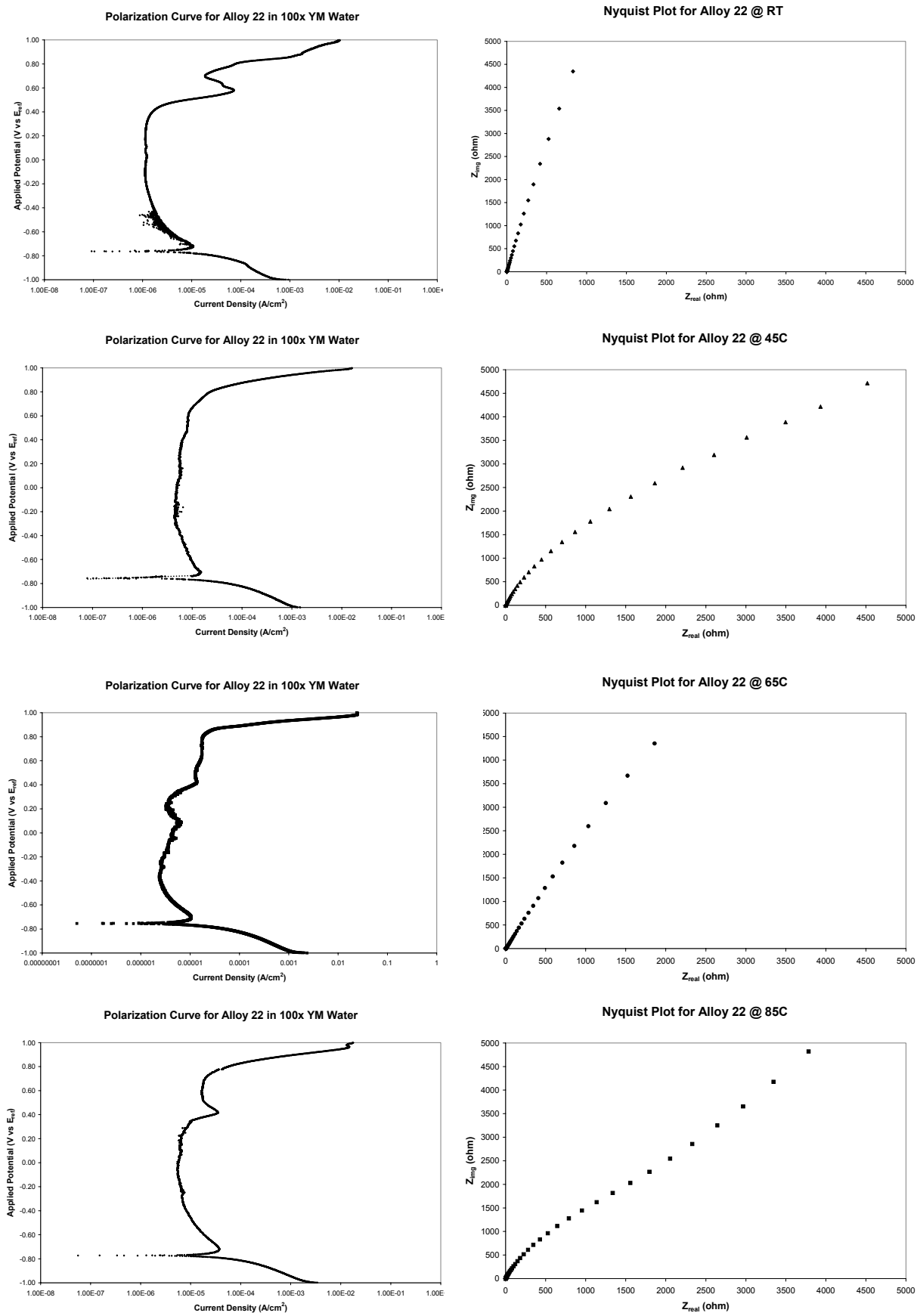

Figure 3.4.3. Polarization Curve (left) and Nyquist Plot (right) for alloy 22 at different

The corrosion rate has been calculated from the corrosion current (I_{corr}) and is listed in Table 3.4.1. A plot of corrosion rate as a function of temperature is shown in figure 3.4.4. From the plot we can see that as the temperature goes up the corrosion rate also goes up. The maximum corrosion rate measured is 14 μm/year at 85° C. A detail study (repeatability tests) is needed to conclude this trend of corrosion rate (CR) data; if the slight decrease in CR rate (5.85 mm/yr.) at 45°C is in fact true. Another study by Evans et. al.[2], using $CaCl_2$ and $CaCl_2$+$Ca(NO_3)_2$ solutions, reported that the maximum corrosion rate of Alloy 22 as 10 μm/year (10 mpy), which is quite low.

Table 3.4.1. Corrosion Rate of Alloy 22 at Different Temperatures 100x simulated YM water under de-aerated conditions.

Temp. (°C)	Temp.(K)	Corrosion Rate (μm/year)	YM Water Concentration
25	298	7.84	100x (Deareated)
45	318	5.88	100x (Deareated)
65	338	9.80	100x (Deareated)
85	358	13.72	100x (Deareated)

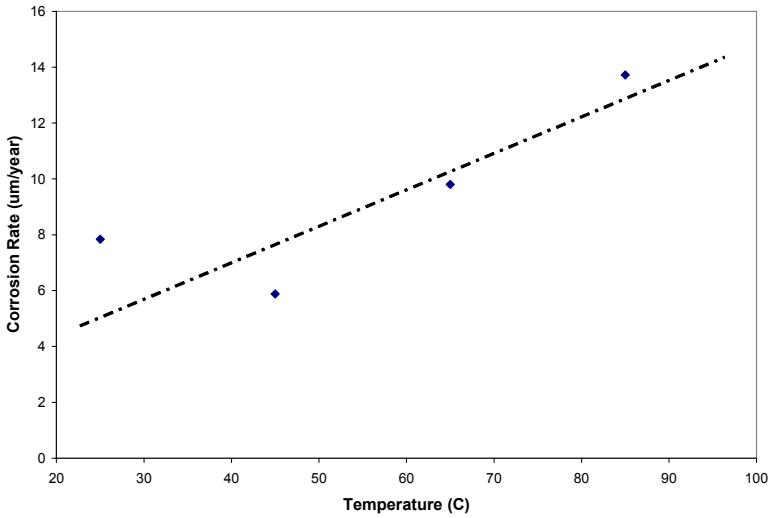

Figure 3.4.4. Corrosion Rate of Alloy 22 as a function of Temperature

References for Section 3.4.

1. http://www.gamry.com/App_Notes/DC_Corrosion/GettingStartedWithEchemCorrMeasurements.htm
2. Kenneth J. Evans, S. Daniel Day, Gabriel O. Lievbare, Michael T. Whalen, Kenneth J. King, Gary A. Hust, Lana L. Wong, John C. Estill and Raul B. Rebak, Transportation, Storage and Disposal of Radioactive Materials, 2003, 55-62.

Time line

For Task ORD-FY04-019 we have started the oxidation tests using TGA, EIS, Potentiodynamic tests, stress corrosion studies, x-ray diffraction analyses and scanning electron microscopy as per timeline. The experimental apparatus for the immersion experiments is being set-up. There has been a delay due to the ongoing review of the Implementation Procedure. The experiments will be underway soon.